Fractal dimension estimation for machine vision applications

H. G. Andrews II & W.E. Foor
RL/OCPA 25 Electronic Parkway, Griffiss AFB, NY 13441-4515

ABSTRACT

This research investigated the use of fractal dimension measure to segment spatially disjoint regions of interest from simulated fractal clutter or background. The underlying assumption is that a given region of interest in a real-world image has a different fractal dimension than its background. We investigated virtually illuminated, digitally simulated fractal surfaces with known fractal dimensions. The backgrounds we considered had various degrees of texture roughness. We constructed an optically based image segmentation system to perform the otherwise computationally intensive Fourier transform of the image to be segmented. We compared the performance of this system to an all digital approach. Though useful for such things as aerial and space based reconnaissance, there are many other applications that could also benefit from the techniques described here. For instance, when applied to machine vision applications, these techniques could help reduce the time required to locate some tool against spatially disjoint clutter. They could also prove useful to applications involving robotic navigation of guidance for hazardous material cleanup. In both cases additional processing will allow the machine to make decisions based on information from a few regions of interest. These techniques could also possibly prove useful as a preprocessor of imagery generated by medical scanners. The rationale is that a growth may have a different fractal dimension than the surrounding tissue. This work was completed at the Photonics Center of Rome Laboratory, Griffiss AFB, NY.

I. INTRODUCTION

Previous theoretical and experimental work[1,2] established a relationship between the topological features of a fractal surface, the surface's illuminated image, and its power spectrum. From these relationships, we estimate a fractal dimension measure from an optical Fourier transform and digital post-processing its power spectrum. From these results, certain inferences can be drawn concerning the location of regions of interest. Namely, the techniques discussed here can quickly spot features having different fractal dimensions from the surrounding clutter.

This investigation compared the ability of an all digital technique to a hybrid optical-digital technique for estimating the fractal dimension of the computer generated imagery. The digital method took a fast Fourier transform of the illuminated image, and used that to calculate the image's fractal dimension. The optical-digital technique did essentially the same thing, though the Fourier transform was taken optically. A Fourier lens, a 256x256 Semetex Magneto-Optic spatial light modulator (SLM) and a CCD camera at the Fourier plane composed the optical system. Once we had the Fourier transform, digital post-processing calculated the fractal dimension of the original illuminated image. This digital post-processing was identical in both the digital system and the hybrid optical-digital system.

II. ALGORITHM

We used the spectral synthesis method to generate fractal surfaces[3]. First, we generated two dimensional random Fourier components $G_{i,j}$ with a mean amplitude of zero and a standard deviation

$$\sigma^2 = \left(i^2 + j^2\right)^{(H+1)/2} \quad \textbf{(1)}$$

on the (i,j)th random discrete Fourier component, where H is related to the desired fractal dimension D[4,5] of the surface by

$$D = 2H \quad (2)$$

A computer performed an inverse Fourier transform to generate a fractal surface $g(x,y)$

$$g(x,y) = \sum_{k=0}^{n-1}\sum_{l=0}^{n-1} G_{k,l}\, e^{2\pi i(kx+ly)} \quad \textbf{(3)}$$

Surface g was illuminated using a pure Lambertian model where the intensity at a particular location $I(x,y)$ is given by:

$$I(x,y) = \cos\left(P_{x,y}\right) \quad \textbf{(4)}$$

where $p_{x,y}$ is the angle between the normal of g at (x_0,y_0) and the direction to the infinitely distant point source illuminant. The normal N_0 at (x_0,y_0) is:

$$\mathbf{(5)} \qquad N_0 = g_x(x_0, y_0)\mathrm{i} + g_y(x_0, y_0)\mathrm{j} - \mathrm{k}$$

We calculated the power spectrum, $P_H(f,t)$ of I by summing the squares of amplitudes within particular frequency rings. The computer then bandpass filtered the power spectrum, plotted it on a log-log graph, and fitted it to a line. A linear relationship exists between the slope of the line $-b$ and the fractal dimension D of the original illuminated image[1,6].

$$\mathbf{(6)} \qquad D = \frac{3 \cdot b}{2}$$

III. SURFACE GENERATION AND ILLUMINATION

Twelve surfaces were created using the spectral synthesis method described above. Illuminating each surface from a variety of angles required knowledge of the normal to the surface at each of the 65,536 points composing the surface. The computer derived the normal of $g(x_0,y_0)$ from the partial derivatives as described in (5) above. To get these partial derivatives we used discrete Fourier transforms to numerically approximate these partial derivatives. This approach was very compute intensive, and limited the number of Fourier components we could use.

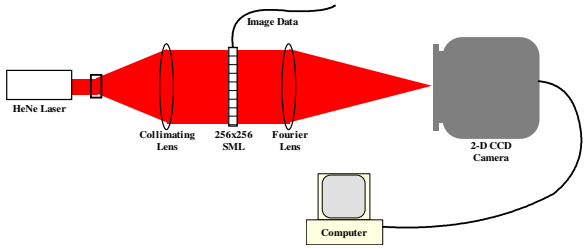

Figure 1 - Optical System Schematic

Six of these twelve surfaces used 16x16 Fourier components and the other six used 32x32 components. For each set of surfaces, we varied the H parameter from 0.0 to 1.0 in increments of 0.2. A computer virtually illuminated each of these twelve surfaces from six angles, and generated simulated imagery as viewed from directly above. The six angles of illumination varied from 0 to 90 degrees relative to the viewing angle. We stored the 72 resulting images in 256x256 BMP format gray scale files.

We should note here that the surfaces images are not self shadowing. To establish certain baseline characteristics of the algorithm and the optical system's performance, we decided to remain consistent with the notions established in previous literature on this subject[1]. Additionally, the surfaces considered followed the properties of a pure Lambertian illumination model for the same reason.

IV. ESTABLISHING BASELINE CHARACTERISTICS

An optical system like that shown in Figure 1 performed a Fourier transform of each of the 72 images. This setup could take the Fourier transform only of binarized images. The Semetex 256x256 SLM used in our experiment is a binary device. As such, we thresholded the grayscale images at their average intensity level before placing them onto the SLM. The Fourier transform of the image on the SLM was imaged onto the CCD camera. A frame grabber card then captured this image into a personal computer. The computer clipped and placed the image from the camera into a binary file for image processing.

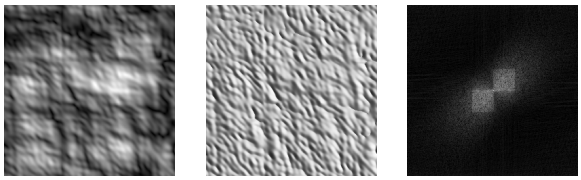

(a) Contour Map (b) Illuminated Image (c) Illuminated Image FT

Figure 2 - Sample Digital Images

The digital technique used the fast Fourier transform (FFT) routines in the Image Pro Plus software package running on a 33MHz 80486DX computer. Image Pro calculated the FFT of all the illuminated surface images and stored the amplitude information in BMP binaries. We discarded the phase information. Each 256x256 Fourier transform required approximately five seconds to compute. Figure 2 shows a typical image from its surface contour map, to its illuminated image, to the image of its FFT. An example of the images taken from the optical system was not easily ported into this paper.

Additional processing calculated the power spectrum of each of the 144 Fourier images and saved the data to ASCII files. To reduce the effects of noise with the optical system (arising mainly from the pixilation of the SLM), we blocked the sections of the optical Fourier transform extending both horizontally and vertically

from the DC. A computer digitally band pass filtered all of the Fourier transforms and graphed the resulting power spectra on a log-log plot.

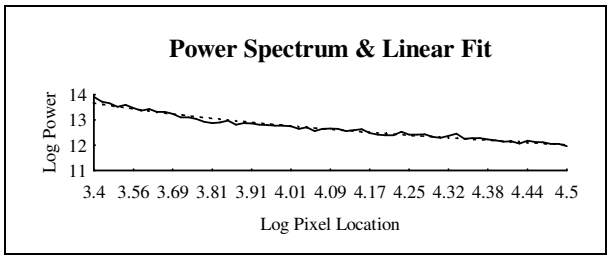

Figure 3 - Power Spectrum Plot

The slope of the line fit to the data in the log-log plots is *-b*. Figure 3 shows a typical example of the power spectrum and its linear fit. We used equation (6) above to calculate *D*. Tables 1 through 4 show the values for *D* in each of the 144 Fourier transforms. The *H* value refers to the parameter for generating the fractal surface, while *t* refers to the angle of the illumination. Except extreme cases in illumination angle or the parameter *H*, the digitally computed values cluster closely to each other for a given fractal dimension. The range of fractal dimension results for a particular value of *H* does not intrude upon the range calculated for another value of *H*, though it does occasionally occur.

V. CHARACTERISTICS WHEN DEVIATING FROM THE BASELINE

In Part IV we considered only nonoccluded fractal surfaces illuminated from a variety of angles. A geometric shape (such as a square) can be placed over part of the illuminated image to see how this changes the fractal dimension measure *D* from the baseline established in Part IV. (See figure 4.) This was done with both a uniformly shaded square covering the middle of the selected images, and with a square region filled with random 8-bit values. (We call them a uniform pulse and a random pulse respectively). Tables 5 through 8 show values for *D* when we employed the two techniques on the two sets of surfaces.

In each case, we handled the images identically to those in Part 4 above, and reduced the data in the same fashion. Due to the large amount of energy in the higher frequencies of the random pulse, the slope increased, decreasing the value of *b* (flattening things out a bit). Similarly, there was a great deal of spectral energy along the axes, (characteristic of sharp edges) and a large value at the DC.

The digital approach seems well suited to differentiate between the two pulse types and the unpulsed data in both the 16x16 and 32x32 Fourier component tests. The difference between the maximum and minimum values is rarely greater than 0.1 save for values of H=1.0. This implies that a deviation greater than 0.1 may show a potential region of interest, and may warrant further investigation by either human or electronic processing. Most of the uniform pulse images were at least 0.1 from all of the unpulsed images with that H value. All of the random pulses were even further away.

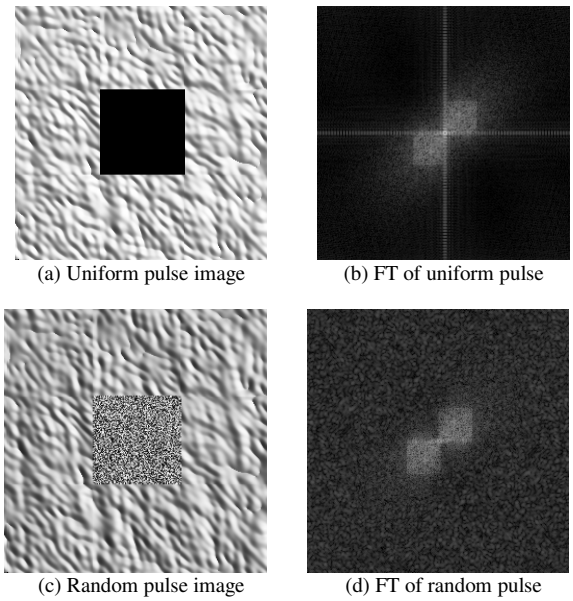

(a) Uniform pulse image (b) FT of uniform pulse

(c) Random pulse image (d) FT of random pulse

Figure 4 - FFT of Occluded Images

Turning our attention to the optical setup, we see that there is a bit of a reduction in the ability to discriminate the random pulse and unpulsed data. However, usually there is still little overlap between the two. Here, we discriminate the uniform pulse much more easily than in the all digital process. The difference in performance characteristics may have been the result of noise in the SLM. Upon viewing the output from the SLM, there were several lines of light, parts of which should have been turned off. Also, the light passing throughout the SLM at the region containing the random pulse did not appear distributed properly. This may have contributed to the poor performance. Pixelation was not as much of a factor as it could have been. As noted earlier, we digitally blocked the axes when calculating the power spectrum. This should have reduced, if not eliminated the effects of pixelation. However, it also removed the spectral energy we expected to see in the uniform pulse.

VI. PERFORMANCE COMPARISON

Each approach described has strengths and weaknesses. The primary advantage of the optical system is that the potential speed is far greater than that offered by any of

the priced digital alternatives. Semetex claims a 50fps frame rate on its 256i. Thus, 250 Fourier transforms can be performed optically in the time it takes to calculate one FFT on the digital platform used here. This assumes that computer hardware controlling the optical system can retrieve imagery at a minimum of 50fps.

There were several disadvantages when using the optical system as well. The optical system seemed more prone to noise, and the Semetex requires a great deal of fine tuning to get the image displayed properly on the device. Incorrect switching of entire rows and columns of pixels, SLM pixelation, and nonuniform illumination of the SLM all combined to produce noise at the detector array. Optical aberrations and imperfect alignment generated crosstalk, further degrading discrimination ability. Additionally, the Semetex often requires more than one write to the array to eliminate large horizontal bands of light from passing through the device. Finally, we failed to match Semetex's 50fps frame rate on the 256i.

The advantages of the digital system involve the ability to reduce the noise levels of the process. Based on the results in the tables below, for a given *H* value, the fractal dimension measure *D* has less variation in the digital system than the optical. FFTs have been sufficiently debugged, and computer performance has become increasingly cost-effective that digital FFTs are offering a serious challenge to the speed benefit derived from optical image processing. This is especially the case when considering the time and resources required to write information to the SLM and read that data back from the CCD array. Also, the digital system does not require throwing away as much information as does the optical system. Digital systems use eight bit gray scale data, while optical systems require us to eliminate seven of those eight bits.

The main disadvantage offered by the digital approach compared with the optical system is the speed. Optical systems have the potential greatly outperform digital systems since they compute Fourier transforms at the speed of light. However, severe bottlenecks exist when writing an image to the SLM and reading its Fourier Transform from the camera. Improvements in optical device and analog to digital conversion technology may overcome with these bottlenecks.

VII. CONCLUSIONS

Based on the performance of the techniques discussed, it is possible to segment square pulses from fractal backgrounds based on the fractal dimension measure. This implies that there is some merit in considering how this approach deals with more sophisticated shapes occluding portions of more realistic scenery. The next logical step in this line of investigation is to look at scanning across high resolution imagery to detect areas where abrupt changes in the fractal dimension occur.

Though the capability to view even small (256x256) optical images in anything approaching a real-time fashion is expensive with the off-the-shelf technology, this technology has applications to other areas in which that capability is not much of a consideration. These techniques could be employed to highlight regions within images taken by various pieces of medical scanning equipment or to automate the process of searching for regions of interest within aerial or space based reconnaissance imagery. If the technology matures sufficiently, applications where timely image processing is critical (such as assembly lines and different robotics applications) will greatly benefit from these techniques.

IX. TABLES

H\t	0°	18°	36°	54°	72°	90°
0.0	2.043	2.005	1.944	1.906	1.905	1.940
0.2	2.123	2.094	2.024	1.973	1.964	2.002
0.4	2.198	2.172	2.102	2.049	2.038	2.070
0.6	2.236	2.231	2.211	2.188	2.183	2.192
0.8	2.011	2.044	2.114	2.140	2.128	2.109
1.0	1.549	1.606	1.739	1.864	1.870	1.793

Table 1 - Digital fractal dimension results *D* for 16x16 Fourier components with parameter *H* and illumination angle *t*

H\t	0°	18°	36°	54°	72°	90°
0.0	1.799	1.819	1.781	1.745	1.744	1.766
0.2	1.91	1.92	1.876	1.832	1.828	1.860
0.4	2.043	2.074	2.033	1.986	1.974	2.002
0.6	2.244	2.307	2.286	2.246	2.230	2.260
0.8	2.261	2.432	2.510	2.522	2.518	2.509
1.0	1.751	2.072	2.311	2.434	2.442	2.351

Table 2 - Digital fractal dimension results *D* for 32x32 Fourier components with parameter *H* and illumination angle *t*

H\t	0°	18°	36°	54°	72°	90°
0.0	1.707	1.765	1.652	1.613	1.704	1.776
0.2	1.745	1.713	1.732	1.685	1.865	1.824
0.4	1.735	1.740	1.700	1.809	1.828	1.844
0.6	1.853	1.791	1.790	1.760	1.805	1.836
0.8	1.845	1.806	1.876	1.823	1.872	1.900
1.0	1.765	1.989	2.013	1.960	1.996	1.965

Table 3 - Optical fractal dimension results *D* for 16x16 Fourier components with parameter *H* and illumination angle *t*

H\t	0°	18°	36°	54°	72°	90°
0.0	1.517	1.803	1.804	1.715	1.651	1.784
0.2	1.503	1.804	1.803	1.581	1.667	1.868
0.4	1.448	1.658	1.494	1.514	1.709	1.837
0.6	1.473	1.459	1.527	1.602	1.784	1.828
0.8	1.402	1.718	1.611	1.752	1.817	1.847
1.0	1.759	1.885	1.814	1.833	1.823	1.873

Table 4 - Optical fractal dimension results *D* for 32x32 Fourier components with parameter *H* and illumination angle *t*

H\t	18°	36°	54°	72°
0.4 (Random)	1.164	1.212	1.248	1.249
0.4 (Uniform)	2.015	1.994	1.979	1.976
0.6 (Random)	1.097	1.124	1.150	1.145
0.6 (Uniform)	1.992	2.018	2.033	2.051

Table 5 - Digital fractal dimension results *D* for 16x16 Fourier components with parameter *H*, illumination angle *t*, and uniform or random pulse as indicated

H\t	18°	36°	54°	72°
0.4 (Random)	1.330	1.418	1.462	1.467
0.4 (Uniform)	1.973	1.969	1.942	1.940
0.6 (Random)	1.233	1.322	1.370	1.370
0.6 (Uniform)	2.071	2.106	2.113	2.126

Table 6 - Digital fractal dimension results *D* for 32x32 Fourier components with parameter *H*, illumination angle *t*, and uniform or random pulse as indicated

H\t	18°	36°	54°	72°
0.4 (Random)	1.688	1.739	1.616	1.590
0.4 (Uniform)	2.183	2.016	1.958	1.960
0.6 (Random)	1.779	1.692	1.681	1.691
0.6 (Uniform)	2.224	2.062	2.037	1.992

Table 7 - Optical fractal dimension results *D* for 16x16 Fourier components with parameter *H*, illumination angle *t*, and uniform or random pulse as indicated

H\t	18°	36°	54°	72°
0.4 (Random)	1.790	1.867	1.832	1.810
0.4 (Uniform)	2.185	2.084	2.066	2.036
0.6 (Random)	2.005	1.870	1.785	1.735
0.6 (Uniform)	2.071	2.106	2.113	2.126

Table 8 - Optical fractal dimension results *D* for 32x32 Fourier components with parameter *H*, illumination angle *t*, and uniform or random pulse as indicated

X. REFERENCES

1. P. Kube, A. Pentland "On the imaging of fractal surfaces" IEEE Transactions on Pattern Analysis and Machine Intelligence, Vol. PAMI-10(5), September 1988.

2. H.G. Andrews II, M.A. Getbehead, S.P. Kozaitis, "Fractal dimension estimation for optical image segmentation" Photonics for Processors, Neural Networks, and Memories, SPIE Proc. 2026, pp 361-370, San Diego, CA, July 1993

3. H.O. Peitgen (Ed) The Science of Fractal Images, Springer-Verlag, Berlin (1988)

4. J. Feders Fractals, Plenum Press, New York, NY (1988)

5. S.P. Kozaitis, H.G. Andrews II, W.E. Foor "Optical image analysis using fractal techniques" Analog Photonics, SPIE Proc. 1790, pp 117-124, Boston, MA, September 1992

6. R.F. Voss, "Random fractal forgeries" Fundamental Algorithms for Computer Graphics, R.A. Earnshaw (Ed), Springer-Verlag, Berlin (1985)